

# Velocity width measurements of the coolest X-ray emitting material in the cores of clusters, groups and elliptical galaxies

J. S. Sanders<sup>1,2</sup> and A. C. Fabian<sup>1</sup>

<sup>1</sup> *Institute of Astronomy, Madingley Road, Cambridge. CB3 0HA*

<sup>2</sup> *Max-Planck-Institute für extraterrestrische Physik, 85748 Garching, Germany.*

13 September 2018

## ABSTRACT

We examine the velocity width of cool X-ray emitting material using *XMM-Newton* Reflection Grating Spectrometer (RGS) spectra of a sample of clusters and group of galaxies and elliptical galaxies. Improving on our previous analyses, we apply a spectral model which accounts for broadening due to the spatial extent of the source. With both conventional and Markov Chain Monte Carlo approaches we obtain limits, or in a few cases measurements, of the velocity broadening of the coolest X-ray material. In our sample, we include new observations targeting objects with compact, bright, line-rich cores. One of these, MACSJ2229.7-2755, gives a velocity limit of  $280 \text{ km s}^{-1}$  at the 90 per cent confidence level. Other systems with limits close to  $300 \text{ km s}^{-1}$  include A 1835, NGC 4261 and NGC 4472. For more than a third of the targets we find limits better than  $500 \text{ km s}^{-1}$ . HCG 62, NGC 1399 and A 3112 show evidence for  $\sim 400 \text{ km s}^{-1}$  velocity broadening. For a smaller sample of objects, we use continuum-subtracted emission line surface brightness profiles to account for the spatial broadening. Although there are significant systematic errors associated with the technique ( $\sim 150 \text{ km s}^{-1}$ ), we find broadening at the level of 280 to  $500 \text{ km s}^{-1}$  in A 3112, NGC 1399 and NGC 4636.

**Key words:** intergalactic medium — X-rays: galaxies: clusters

## 1 INTRODUCTION

Measuring the velocity distribution of the intracluster medium (ICM) in clusters and groups of galaxies and in elliptical galaxies is important for understanding how such structures form and the strength of active galactic nucleus (AGN) feedback. Simulations of AGN feedback imply the creation of ICM velocity widths of several hundred  $\text{km s}^{-1}$  (Brüggen et al. 2005; Heinz et al. 2010). In addition, sloshing of gas within the potential well of a cluster can give rise to similar velocities (Ascasibar & Markevitch 2006). Cosmologically generated turbulence is expected to be a relatively small 5 to 15 per cent fraction of the thermal energy density in the cores of galaxy clusters (Lau et al. 2009; Vazza et al. 2009, 2011),

The most direct method for measuring or placing limits on velocities on clusters is examining X-ray emission line widths. This was first done by examining a deep X-ray grating spectrum of A 1835 taken using the RGS (Reflection Grating Spectrometer) instruments on *XMM-Newton* (Sanders et al. 2010b). We followed this up with a study a sample of bright emission line objects (Sanders et al. 2011). As the RGS spectrometers are slitless spectrometers, the extent of the source contributes to the line width. For our most conservative analysis we assumed that the objects were point sources, and therefore obtained upper limits on the velocity broadening. For A 1835 we measured a 90 per cent confidence upper limit of  $274 \text{ km s}^{-1}$  and less than  $500 \text{ km s}^{-1}$  for several objects in our sample. In A 1835 the upper limit corresponds to the

fraction of energy in turbulence of less than 13 per cent of the thermal energy density.

Other objects have recently been examined. Bulbul et al. (2012) analysed *XMM* observations of A 3112. Their most conservative upper limit was around  $900 \text{ km s}^{-1}$ . de Plaa et al. (2012) recently examined two elliptical galaxies. Using resonance scattering to provide lower limits and line widths to find upper limits they obtain  $320 < V_{\text{turb}} < 720 \text{ km s}^{-1}$  for NGC 5044 and  $140 < V_{\text{turb}} < 540 \text{ km s}^{-1}$  for NGC 5813.

In Sanders et al. (2010b) we went on to account for spectral broadening due to the spatial extent of A 1835. Using an *Chandra* image of the cluster in the Fe-L band we reduced our limit to  $\sim 180 \text{ km s}^{-1}$ . In addition, Bulbul et al. (2012) used *XMM* images to account for the surface brightness of A 3112, finding improved limits of  $\sim 200 \text{ km s}^{-1}$ .

When analysing the sample of objects in Sanders et al. (2011), we also applied an experimental technique of modelling RGS spectra using spatially-resolved *Chandra* maps of the sources, comparing the real line widths with predicted ones. This method had a number of systematic issues: using projected quantities, not including the uncertainties in the maps, assuming Solar abundance ratios and the finite sizes of the bins used. It has also been pointed out by M. Markevitch that we did not subtract our modelled line widths in quadrature from the observed line widths.

In this paper, we improve on our previous analyses to take ac-

arXiv:1212.1259v1 [astro-ph.CO] 6 Dec 2012

count of the spatial broadening in a robust manner. Firstly, we fit the RGS spectra, modelling the spatial distribution of the source. For some selected sources, we go on to use emission line profiles along the dispersion direction, subtracting continuum emission, to include the effects of the spatial broadening. We find a number of strong upper limits, but for a few sources we are able to find moderate detections of line broadening due to gas motions.

The Solar abundance ratios of Anders & Grevesse (1989) are used in this paper. Velocity values quoted are the Gaussian width,  $\sigma$ .

## 2 SPECTRAL ANALYSIS

The line width measured in an RGS spectrum includes the intrinsic line width from random or turbulent velocities and thermal motions. The thermal motion is included within the spectral model and is therefore accounted for during spectral fitting. The non-intrinsic contribution includes the instrumental line width (accounted for within the response) and the spectral broadening due to the extent of the source. The RGS instruments do not have slits, so the size of the source broadens the spectrum by

$$\Delta\lambda \approx \frac{0.139}{m} \Delta\theta \text{ \AA}, \quad (1)$$

where  $m$  is the spectral order and  $\Delta\theta$  is the half energy width of the source in arcmin (note that the incorrect factor 0.124 is given in some works, including Brinkman et al. 1998). In our previous analyses we placed an upper limit on the line width, putting a constraint on the velocity broadening.

The contribution to broadening from the spatial component is a fixed broadening in wavelength. Velocity broadening gives a fractional broadening in energy or frequency. In principle, if we include a spectral model which characterises the fixed  $\delta\lambda$  broadening from the extent, we can also determine the velocity broadening independently. If the data quality is too low we can constrain a combination of the size and velocity.

In order to test whether this was possible we examined simulated spectra. 1st and 2nd order *XMM* RGS1 and 2 response matrices were created with the *SAS* RGSRMFGEN tool. We supplied a custom Gaussian angular distribution with width  $\sigma = 0.3$  arcmin. Spectra were simulated with these responses in *XSPEC* (Arnaud 1996) using a 1.5 keV *BVAPEC* model,  $0.5 Z_{\odot}$  metallicity and including  $500 \text{ km s}^{-1}$  Doppler broadening. We took these simulated spectra and fit them using a point-source response matrix, a *BVAPEC* model, but convolved with a Gaussian with a fixed width in wavelength (parameterised by an angular scale, as in equation 1). We were able to recover the broadening velocity and Gaussian width of the source,  $\sigma$ , when fitting.

### 2.1 Simple spatial modelling

The data were prepared using the methods described in Sanders et al. (2011). We used the same 90 per cent of the point spread function (PSF) extraction region in the cross-dispersion direction and 90 per cent of the pulse height distribution. This selection region corresponds roughly to a 50 arcsec strip across the cluster in the cross-dispersion direction. Background spectra were extracted outside 98 per cent of the PSF. There have been some changes to the datasets included. We list the datasets used in Table 1. These data include observations of new objects such as MACS J2229.7-2755 (see Fig. 1). We have removed some of the poorer quality datasets

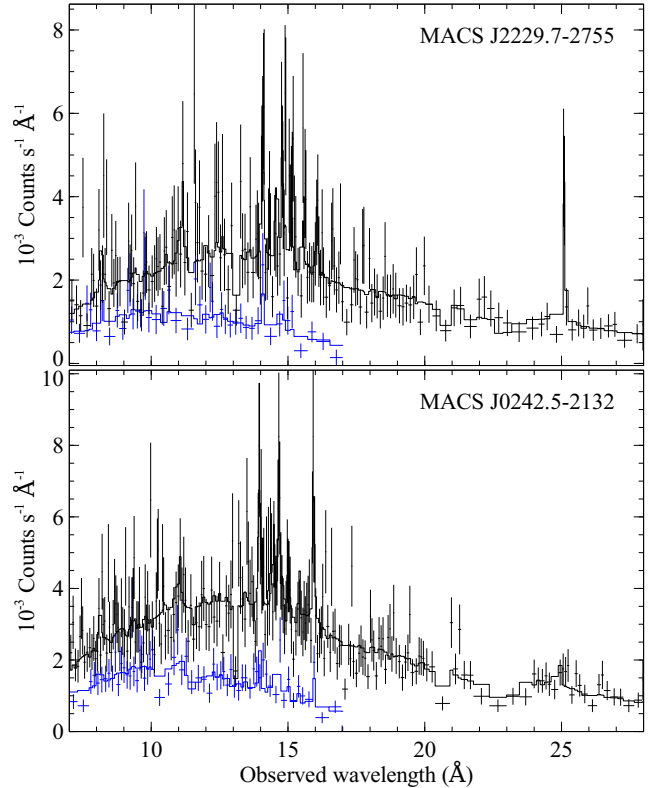


**Figure 1.** RGS spectra of two new observations of MACS clusters included in this paper. The data were rebinned for MACS J2229.7-2755 and MACS J0242.5-2132 to a minimum signal to noise ratio of 3 and 4, respectively. We note that MACS J0242.5-2132 does not show the obvious narrow O VIII emission line as seen in MACS J2229.7-2755. This appears to be due to a combination of a lower best-fitting oxygen metallicity ( $0.15 \pm 0.08$  vs  $0.44^{+0.18}_{-0.11} Z_{\odot}$ ), broader emission lines and higher absorbing column density. The two clusters have similar temperatures, fluxes and redshifts.

from the sample, in particular those where the background was a large fraction of the spectrum or the emission lines were weak. The datasets were reprocessed to take advantage of the updated calibration of the RGS line-spread function (*XMM*-CCF-REL-275). In addition, we increased the number of rows in the response matrices from the default value of 4000 to 16000.

For most of the objects we fitted a single component *BVAPEC* spectral model (i.e. an APEC thermal model with variable abundances, thermal broadening and variable Gaussian broadening). The APEC model (Smith et al. 2001) we used was recreated from the APED 2.0.2 database with a temperature grid size of 0.01 dex, rather than using the default 0.1 dex tables. The PHABS photoelectric absorber component (Balucinska-Church & McCammon 1992) was applied to this model. We convolved the absorbed thermal model with a Gaussian of a constant wavelength width, parameterised as the spatial scale. The data were fit in the *XSPEC* spectral analysis package, minimising the C-statistic during fitting. We fit the spectra between 7 and  $28 \text{ \AA}$  for the first order data and 7 to  $17 \text{ \AA}$  for the second order spectra.

We note that using a spectral background extracted off-axis from the dataset itself may not be correct and depends on the source morphology and structure. If most of the flux from the object is emitted from within the extraction region, the background components will be correctly subtracted using off axis regions. If the source is more extended than the background region, the back-

**Table 1.** Details of the examined objects and datasets. Listed are the object names, redshifts, extraction position in decimal degrees (J2000), mean cleaned RGS 1 and 2 exposure and *XMM* datasets.

Object	Redshift	RA	Dec	Exposure (ks)	<i>XMM</i> observations
2A 0335+096	0.0349	54.6713	9.9669	117.1	0147800201
A1068	0.1375	160.1855	39.9529	22.6	0147630101
A133	0.0566	15.6740	-21.8805	24.0	0144310101
A1795	0.0625	207.2182	26.5937	40.5	0097820101
A1835	0.2523	210.2580	2.8787	220.6	0098010101 0551830101 0551830201
A1991	0.0587	223.6318	18.6449	40.4	0145020101
A2029	0.0773	227.7339	5.7446	172.1	0111270201 0551780201 0551780301 0551780401 0551780501
A2052	0.0355	229.1855	7.0214	116.7	0109920101 0401520301 0401520501 0401520601 0401520801 0401520901 0401521101 0401521201 0401521601 0401521701
A2204	0.1522	248.1957	5.5753	85.9	0112230301 0306490101 0306490201 0306490301 0306490401
A2597	0.0852	351.3324	-12.1243	84.0	0108460201 0147330101
A262	0.0163	28.1924	36.1528	127.7	0109980101 0504780101 0504780201
A2626	0.0553	354.1272	21.1467	55.6	0083150201 0148310101
A3112	0.075252	49.4902	-44.2381	203.3	0105660101 0603050101 0603050201
A3581	0.023	211.8741	-27.0183	137.8	0205990101 0504780301 0504780401
A383	0.1871	42.0140	-3.5291	32.3	0084230501
A4059	0.0475	359.2542	-34.7591	46.6	0109950101 0109950201
A496	0.0329	68.4077	-13.2616	149.5	0135120201 0506260301 0506260401
AS1101	0.058	348.4948	-42.7263	98.0	0147800101
Centaurus	0.0114	192.2039	-41.3125	157.7	0046340101 0406200101
E 1455+2232	0.2578	224.3129	22.3424	36.1	0108670201
HCG 62	0.0137	193.2738	-9.2042	156.9	0112270701 0504780501 0504780601
Hercules A	0.154	252.7841	4.9924	119.8	0401730101 0401730201 0401730301
Hydra A	0.0539	139.5249	-12.0955	93.5	0504260101
MACS J0242.5-2132	0.314	40.6497	-21.5406	69.0	0673830101
MACS J2229.7-2755	0.324	337.4385	-27.9270	46.8	0651240201
MKW 3s	0.045	230.4662	7.7088	32.6	0109930101
MS 0735.6+7421	0.216	115.4344	74.2440	55.2	0303950101
MS 2137.3-2353	0.313	325.0632	-23.6612	63.9	0673830201
NGC 1316	0.00587	50.6738	-37.2079	159.4	0302780101 0502070201
NGC 1365	0.005457	53.4016	-36.1416	111.6	0505140401
NGC 1399	0.0046	54.6212	-35.4506	126.0	0400620101
NGC 1404	0.00649	54.7156	-35.5946	41.9	0304940101
NGC 1550	0.012389	64.9080	2.4100	25.3	0152150101
NGC 2300	0.007	113.0821	85.7093	52.5	0022340201
NGC 3411	0.0153	162.6087	-12.8451	24.1	0146510301
NGC 4261	0.00706	184.8468	5.8249	94.6	0502120101
NGC 4325	0.02571	185.7776	10.6210	21.1	0108860101
NGC 4472	0.00332	187.4449	8.0008	83.6	0200130101
NGC 4636	0.00313	190.7080	2.6876	57.7	0111190701
NGC 4649	0.00373	190.9165	11.5527	76.0	0502160101
NGC 499	0.01467	20.7985	33.4607	49.1	0501280101
NGC 5044	0.00928	198.8498	-16.3854	133.7	0037950101 0554680101
NGC 533	0.01739	21.3808	1.7592	34.2	0109860101
NGC 5813	0.0066	225.2969	1.7020	162.3	0302460101 0554680201 0554680301
NGC 5846	0.0057	226.6223	1.6049	37.9	0021540101 0021540501
RBS 540	0.0397	66.4636	-8.5601	41.1	0300210401
RBS 797	0.354	146.8029	76.3871	17.7	0502940301
RXC J0605.8-3518	0.141	91.4749	-35.3026	24.1	0201901001
RXC J1044.5-0704	0.1323	161.1369	-7.0691	28.9	0201901501
RXC J1141.4-1216	0.1195	175.3518	-12.2777	29.5	0201901601
RXC J1504.1-0248	0.2153	226.0309	-2.8044	38.9	0401040101
RXC J2014.8-2430	0.1612	303.7154	-24.5057	26.4	0201902201
RXC J2149.1-3041	0.1179	327.2822	-30.7013	26.8	0201902601
RX J1720.1+2638	0.164	260.0414	26.6248	69.2	0500670201 0500670301 0500670401
RX J2129.6+0005	0.235	322.4164	0.0886	43.5	0093030201
Zw3146	0.2906	155.9152	4.1865	209.6	0108670101 0605540201 0605540301

ground will contain source emission. The extraction region is a strip across the cluster and will contain emission from regions outside the core. Using an adjacent strip as background (as we obtain from the off-axis data) will remove much of this outer emission. This spectral component, as it comes from a more extended region will be more highly broadened than that from the source region. We are only interested in the best measurements from the centre, so it is favourable to remove the outer emission. This will particularly be the case for a cool core embedded in a hotter medium. However, there are cases where the geometry of the source may make this subtraction invalid, particularly if the source is not symmetric in the extraction regions. For some objects it would be better to use background spectra from blank sky observations. We also redo the fits using template backgrounds generated with the RGSBKGMODEL tool to check the robustness of our backgrounds.

We allowed the temperature, absorption, redshift, velocity broadening, spatial broadening, normalisation and some metallicities to be free in the spectral fits. The metals which we allowed to be free depended on the temperature of the object and whether there was any continuum in the spectrum. For some objects with high quality data or when required we fitted more than one broadened thermal component, to allow for more than one temperature or spatial scale. The parameters which were allowed to be free during the spectral fitting for each object are shown in Table 2.

We examined the uncertainties in the parameters to the fits using both a conventional approach of varying the parameter until the fit statistic increases from the minimum by the required amount (referred to here as  $\delta C$ ) and using Markov Chain Monte Carlo (MCMC). Rather than use the standard Metropolis-Hastings MCMC algorithm, we used an affine-invariant MCMC sampler (Goodman & Weare 2010) as implemented in EMCEE<sup>1</sup> (Foreman-Mackey et al. 2012). We created a package based on EMCEE to analyse X-ray spectral models and data in parallel invocations of XSPEC<sup>2</sup>. The advantage of an affine-invariant sampler over the Metropolis-Hastings algorithm is that it can sample complex parameter space much more efficiently without any tuning of a proposal distribution. It uses a number of ‘walkers’ which simultaneously examine parameter space within each step on the chain. The proposal distribution for a particular walker depends on the position of the other walkers.

We started the walkers in a small cluster around the best fitting parameter values. 200 walkers were typically used, with a chain length of 2000 (per walker) following a burn-in period of 400. Repeat fractions of the chains after burn-in ranged between 65 and 77 per cent. For some objects, we found discrepancies between the MCMC and  $\delta C$  statistic approaches or there were problems in the convergence of the chain. In these cases we used 4000 walkers, but decreased the length of the chain to 1000 and the burn-in period to 200 to finish the analysis in a reasonable time period (Table 3 lists the number of walkers). When analysing the posterior probability distributions we use all of the walkers. The mean autocorrelation time of the velocity parameter for the walkers are typically less than 3 per cent of the chain length and at worst 6 per cent of the chain length. We also examined the chains by eye to look for problems in the convergence.

In Table 3 are presented the broadening results for each of the objects. The first two columns show the  $1\sigma$  and 90 per cent uncertainties (or limits) on the line-of-sight velocity obtained by allow-

**Table 2.** Spectral fitting parameters used when fitting spectra.  $N_T$  is the number of temperature components used when fitting the spectra and  $N_S$  is the number of spatial components. If two spatial and temperature components are listed, two spatial components with independent temperatures were fitted. The listed metallicities were allowed to vary independently. If Fe is not listed, it was frozen at the Solar value because of a lack of continuum. Unlisted metals were tied to the Fe Solar ratio, except for He which was frozen at the Solar ratio. In addition to these parameters, we allowed the absorbing column density, normalisation (for each temperature component or spatial component), redshift and velocity width to vary.

Object	$N_T$	$N_S$	Metallicities
2A 0335+096	1	1	O Ne Mg Si Fe Ni
A1068	1	1	O Ne Mg Si Fe Ni
A133	1	1	O Ne Mg Fe Ni
A1795	1	1	O Ne Mg Si Fe Ni
A1835	1	1	O Ne Mg Si Fe Ni
A1991	1	1	O Ne Mg Si Fe Ni
A2029	1	1	O Ne Mg Si Fe Ni
A2052	1	1	O Ne Mg Fe Ni
A2204	1	1	O Ne Mg Si Fe Ni
A2597	1	1	O Ne Mg Fe Ni
A262	2	2	O Ne Mg Si Fe Ni
A2626	1	1	O Ne Mg Si Fe Ni
A3112	1	1	O Ne Mg Si Fe Ni
A3581	2	2	O Ne Mg Fe Ni
A383	1	1	O Ne Mg Si Fe Ni
A4059	1	1	O Ne Mg Fe Ni
A496	1	1	O Ne Mg Fe Ni
AS1101	1	1	O Ne Mg Si Fe Ni
Centaurus	2	2	O Ne Mg Fe Ni
E 1455+2232	1	1	O Mg Si Fe
HCG 62	2	2	N O Ne Mg Fe Ni
Hercules A	1	1	O Ne Mg Si Fe Ni
Hydra A	1	2	O Ne Mg Fe Ni
MACS J0242.5-2132	1	1	O Ne Mg Si Fe Ni
MACS J2229.7-2755	1	1	O Ne Mg Si Fe Ni
MKW 3s	1	1	O Ne Mg Si Fe Ni
MS 0735.6+7421	1	1	O Ne Mg Si Fe Ni
MS 2137.3-2353	1	1	O Ne Mg Si Fe Ni
NGC 1316	1	1	O Ne Mg Fe Ni
NGC 1365	1	1	O Ne Mg Fe Ni
NGC 1399	1	1	N O Ne Mg Fe Ni
NGC 1404	1	1	O Ne Mg Fe Ni
NGC 1550	1	1	O Ne Mg Fe Ni
NGC 2300	1	1	O Ne Mg Ni
NGC 3411	1	1	O Ne Mg Fe Ni
NGC 4261	1	1	O Ne Mg Fe Ni
NGC 4325	1	1	O Ne Mg Ni
NGC 4472	1	1	O Ne Mg Fe Ni
NGC 4636	1	1	O Ne Mg Fe Ni
NGC 4649	1	2	O Ne Mg Fe Ni
NGC 499	1	1	O Ne Mg Fe Ni
NGC 5044	1	2	O Ne Mg Fe Ni
NGC 533	1	1	O Ne Mg Ni
NGC 5813	2	2	N O Ne Mg Fe Ni
NGC 5846	1	1	O Ne Mg Ni
RBS 540	1	1	O Ne Mg Si Fe Ni
RBS 797	1	1	O Ne Mg Fe
RXC J0605.8-3518	1	1	O Ne Mg Si Fe Ni
RXC J1044.5-0704	1	1	O Ne Mg Si Fe Ni
RXC J1141.4-1216	1	1	O Ne Mg Fe
RXC J1504.1-0248	1	1	O Ne Mg Si Fe Ni
RXC J2014.8-2430	1	1	O Ne Mg Si Fe
RXC J2149.1-3041	1	1	O Ne Mg Si Fe
RX J1720.1+2638	1	1	O Ne Mg Si Fe Ni
RX J2129.6+0005	1	1	O Mg Si Fe Ni
Zw3146	1	1	O Ne Mg Si Fe Ni

<sup>1</sup> See <http://danfm.ca/emcee/>

<sup>2</sup> Available at [https://github.com/jeremysanders/xspec\\_emcee](https://github.com/jeremysanders/xspec_emcee)

**Table 3.** Velocity broadening results from the change in fit statistic ( $\delta C$ ), both with standard off-axis and template backgrounds, and from the MCMC analysis. We show  $1\sigma$  and 90 per cent confidence uncertainties ( $\text{km s}^{-1}$ ). The number of walkers used in the MCMC analysis is listed. We also show the temperature from the MCMC analysis, with  $1\sigma$  uncertainties. If more than one temperature component was used, this is the value of the higher component. A blank MCMC result indicates that the limit was greater than  $5000 \text{ km s}^{-1}$ .

Object	$\delta C$ ( $1\sigma$ )	$\delta C$ (90 per cent)	$\delta C$ Template ( $1\sigma$ )	$\delta C$ Template (90 per cent)	MCMC ( $1\sigma$ )	MCMC (90 per cent)	MCMC walkers	Temperature (keV)
2A 0335+096	< 190	< 300	< 210	< 330	< 200	< 300	200	$1.58 \pm 0.02$
A1068	< 490	< 710	< 350	< 570	< 480	< 760	200	$2.89^{+0.43}_{-0.38}$
A133	< 420	< 580	$490^{+160}_{-150}$	$490^{+280}_{-250}$	< 380	< 540	200	$3.12^{+0.59}_{-0.42}$
A1795	< 550	< 800	< 500	< 750	< 580	< 880	200	$3.35^{+0.41}_{-0.32}$
A1835	< 240	< 310	< 220	< 290	< 200	< 300	200	$4.58^{+0.57}_{-0.49}$
A1991	< 390	< 460	< 380	< 490	$210^{+110}_{-170}$	< 400	200	$1.68 \pm 0.06$
A2029	< 410	< 480	< 470	< 530	$270^{+70}_{-230}$	< 420	200	$3.82^{+0.44}_{-0.29}$
A2052	< 550	< 700	$400^{+220}_{-340}$	$400 \pm 370$	< 440	< 640	200	$1.72 \pm 0.03$
A2204	< 440	< 520	$330^{+110}_{-230}$	< 510	$310^{+130}_{-190}$	< 480	200	$3.68^{+0.46}_{-0.33}$
A2597	$460^{+190}_{-430}$	< 750	< 580	< 680	$550^{+130}_{-310}$	$550^{+170}_{-510}$	200	$2.92^{+0.25}_{-0.21}$
A2626	< 470	< 670	< 690	< 900	< 440	< 660	4000	$3.49^{+0.88}_{-0.57}$
A262 <sup>2</sup>	< 400	< 570	< 590	< 680	< 400	< 560	200	$1.41^{+0.04}_{-0.04}$
A3112	$420^{+100}_{-140}$	$420^{+150}_{-270}$	$440^{+100}_{-150}$	$440^{+160}_{-310}$	$430^{+110}_{-130}$	$430^{+150}_{-270}$	200	$3.11^{+0.13}_{-0.12}$
A3581 <sup>2</sup>	< 300	< 460	< 400	< 590	< 280	< 420	200	$1.41^{+0.03}_{-0.02}$
A383	< 450	< 690	< 480	< 740	< 480	< 780	4000	$3.61^{+0.85}_{-0.65}$
A4059	$940^{+370}_{-690}$	< 1520	$940^{+350}_{-500}$	< 1470	$1050^{+390}_{-550}$	< 1540	4000	$2.69^{+0.43}_{-0.29}$
A496	< 550	< 690	$540^{+200}_{-330}$	< 850	< 460	< 640	200	$2.19^{+0.06}_{-0.06}$
AS1101	< 290	< 440	< 310	< 420	< 280	< 440	200	$2.24^{+0.08}_{-0.07}$
Centaurus <sup>2</sup>	< 250	< 340	< 370	< 450	< 240	< 340	200	$1.57 \pm 0.02$
E 1455+2232	< 180	< 300	< 220	< 350	< 260	< 540	4000	$3.36^{+1.11}_{-0.56}$
HCG 62 <sup>2</sup>	$390^{+110}_{-120}$	$390^{+170}_{-220}$	$460 \pm 80$	$460 \pm 140$	$390^{+130}_{-150}$	$390^{+190}_{-290}$	200	$0.93^{+0.02}_{-0.02}$
Hercules A	< 810	< 1070	< 770	< 1050	< 800	< 1060	4000	$4.83^{+1.27}_{-1.16}$
Hydra A <sup>2</sup>	$500^{+160}_{-230}$	< 810	$480^{+200}_{-210}$	< 800	$490^{+210}_{-270}$	$490^{+290}_{-450}$	200	$3.09^{+0.26}_{-0.22}$
MACS J0242.5-2132	< 450	< 560	< 470	< 570	$330^{+170}_{-290}$	< 600	200	$4.89^{+1.04}_{-0.98}$
MACS J2229.7-2755	< 150	< 240	< 180	< 280	< 180	< 280	200	$3.80^{+0.73}_{-0.63}$
MKW 3s	< 560	< 870	< 970	< 1480	< 760	< 1220	4000	$3.04^{+0.37}_{-0.27}$
MS 0735.6+7421	< 370	< 540	< 200	< 360	< 780	< 1360	4000	$4.46^{+1.58}_{-1.13}$
MS 2137.3-2353	$460 \pm 200$	$460^{+330}_{-370}$	$420^{+210}_{-220}$	< 750	$390^{+190}_{-370}$	< 800	200	$6.18^{+1.17}_{-1.08}$
NGC 1316	< 250	< 420	< 460	< 560	< 320	< 440	200	$0.64 \pm 0.01$
NGC 1365	< 350	< 460	< 440	< 490	< 340	< 420	200	$0.54^{+0.04}_{-0.05}$
NGC 1399	$380^{+90}_{-130}$	$380^{+130}_{-260}$	$520^{+50}_{-60}$	$520^{+90}_{-90}$	$390^{+90}_{-110}$	$390^{+130}_{-250}$	200	$0.88^{+0.01}_{-0.01}$
NGC 1404	< 330	< 530	< 340	< 520	< 360	< 600	200	$0.64 \pm 0.01$
NGC 1550	< 990	< 1550	< 1120	< 1620	< 980	< 1760	4000	$1.12^{+0.02}_{-0.03}$
NGC 2300	< 240	< 390	< 360	< 590	< 280	< 480	200	$0.69 \pm 0.02$
NGC 3411	< 630	< 950	< 770	< 980	< 700	< 1100	200	$0.89^{+0.02}_{-0.02}$
NGC 4261	< 230	< 330	< 350	< 390	< 200	< 300	200	$0.71 \pm 0.01$
NGC 4325	< 600	< 760	< 380	< 570	< 620	< 700	200	$0.86^{+0.01}_{-0.02}$
NGC 4472	< 140	< 220	< 150	< 240	< 140	< 240	200	$0.82 \pm 0.01$
NGC 4636	< 450	< 550	< 480	< 580	$270^{+130}_{-230}$	< 500	200	$0.63^{+0.01}_{-0.01}$
NGC 4649 <sup>2</sup>	< 320	< 400	< 280	< 360	< 280	< 400	200	$0.85 \pm 0.01$
NGC 499	< 1190	< 1850	< 2210	< 2630	< 1240	< 1940	4000	$0.73 \pm 0.02$
NGC 5044 <sup>2</sup>	< 470	< 570	$400^{+150}_{-300}$	< 630	$370^{+110}_{-270}$	< 540	200	$0.82 \pm 0.01$
NGC 533	< 230	< 380	< 360	< 530	< 280	< 420	200	$0.81 \pm 0.02$
NGC 5813 <sup>2</sup>	$360^{+180}_{-280}$	< 620	$450^{+160}_{-200}$	< 680	$430^{+130}_{-230}$	< 580	200	$0.73^{+0.01}_{-0.01}$
NGC 5846	< 330	< 480	< 500	< 630	< 320	< 480	200	$0.66^{+0.02}_{-0.01}$
RBS 540	$390^{+150}_{-160}$	$390^{+250}_{-340}$	$570^{+150}_{-130}$	$570^{+260}_{-220}$	< 500	< 580	200	$2.52^{+0.23}_{-0.18}$
RBS 797	< 340	< 540	< 410	< 720	< 2500		4000	$5.24^{+1.57}_{-1.27}$
RX J1720.1+2638	< 380	< 730	< 480	< 820	< 600	< 1040	4000	$5.36^{+1.29}_{-1.05}$
RX J2129.6+0005	< 270	< 1780	< 460	< 1600	< 600	< 1580	200	$5.00^{+1.18}_{-1.06}$
RXC J0605.8-3518	< 300	< 490	< 340	< 520	< 380	< 640	4000	$6.11^{+1.06}_{-1.61}$
RXC J1044.5-0704	$20 \pm 490$	< 730	< 530	< 710	< 500	< 880	4000	$3.43^{+0.71}_{-0.56}$
RXC J1141.4-1216	< 280	< 480	< 300	< 490	< 360	< 600	4000	$2.04^{+0.22}_{-0.16}$
RXC J1504.1-0248	$670^{+600}_{-360}$	$670^{+950}_{-630}$	$800^{+480}_{-530}$	< 1570	$1310^{+570}_{-670}$	$1310^{+970}_{-1090}$	4000	$6.22^{+1.58}_{-1.23}$
RXC J2014.8-2430	< 200	< 420	< 330	< 750	< 480	< 820	4000	$7.86 \pm 1.43$
RXC J2149.1-3041	< 200	< 310	< 230	< 350	< 220	< 360	200	$2.67^{+0.95}_{-0.39}$
Zw3146	$310^{+90}_{-100}$	$310^{+150}_{-170}$	$310 \pm 90$	$310 \pm 150$	$290^{+70}_{-250}$	< 420	200	$3.94^{+0.54}_{-0.44}$

ing the fit statistic to increase by 1.0 or 2.71, respectively. These are followed by the same results when template background spectra are used. The next two columns show the same results obtained from the MCMC analysis. It is unclear how to calculate an error bar or limit from MCMC when a parameter is close to a hard limit ( $0 \text{ km s}^{-1}$  broadening here), relative to its uncertainty. Normally one would take the median value of a parameter and its percentiles from the chain. If the posterior probability distribution is significant at a limit then using a percentile to compute uncertainties will give finite values, rather than a value consistent with that limit. As many of our velocities are limits, we therefore used a different technique examining the marginalised posterior probability distribution. This distribution was computed for the velocity broadening in 250 linear velocity bins up to  $5000 \text{ km s}^{-1}$ . We selected the most likely velocity (this is the quoted value when significant). We moved down to lower values of marginalised probability until the required integrated probability was obtained. The error bar that we quote are the minimum and maximum values of velocity that bound this integrated probability region.

We plot our values and uncertainties from the standard and MCMC methods for each object in Fig. 2. It can be seen that for most of the targets that we obtain good agreement between the two methods. However, there are a few cases in which they do not show consistent results. These include RBS 797, where examination of the MCMC chain shows a long tail on the velocity posterior distribution to high velocities and a secondary minimum in the fit statistic at high velocities. MS 0735.6+7421 shows a similar tail to high velocities, but the limit we can obtain is tighter. The tail on E 1455+2232 and RXC J2014.8-2430 are also longer than expected from the  $\delta C$  analysis. The two methods agree for RXC J1504.1-0248 at the  $1\sigma$  level. Some objects show rather poor constraints (e.g. NGC 499). Using template backgrounds makes little difference to the results for most objects, although the change can be  $\sim 200 \text{ km s}^{-1}$ . The worst cases include NGC 499 and MKW 3s, where the discrepancies are  $600 - 800 \text{ km s}^{-1}$ .

In the determination of the broadening of the emission lines the main uncertainty is the extent of the source. We show in Fig. 3 the MCMC posterior probability contours of the velocity and spatial broadening for four objects. It can be seen that there is, of course, some degeneracy between the velocity and spatial broadening. However, this is not complete, as can be seen in A 3112 and NGC 1399.

In Fig. 4 we plot the temperature of each object against the best-fitting velocity ( $1\sigma$  uncertainties, determining the quantities using MCMC).

## 2.2 Incorporation of *Chandra* imaging

The most obvious improvement to our method of fitting for the spatial extent of the source, is to use an X-ray image of the object from *Chandra* or *XMM* to measure the spatial broadening which should be included when modelling the spectrum. The profile of the image along the RGS dispersion direction is examined to compute how the spectrum is broadened. Either a wide band or narrower Fe-L band image could be used. X-ray CCD images have poor spectral resolution, so truly narrow band images cannot be made. Previously we used the RGSXSRC model in *XSPEC* to account for the spatial broadening in A 1835 (Sanders et al. 2010b). Bulbul et al. (2012) used MOS images and RGSRMFSMOOTH to account for source extent in A 3112.

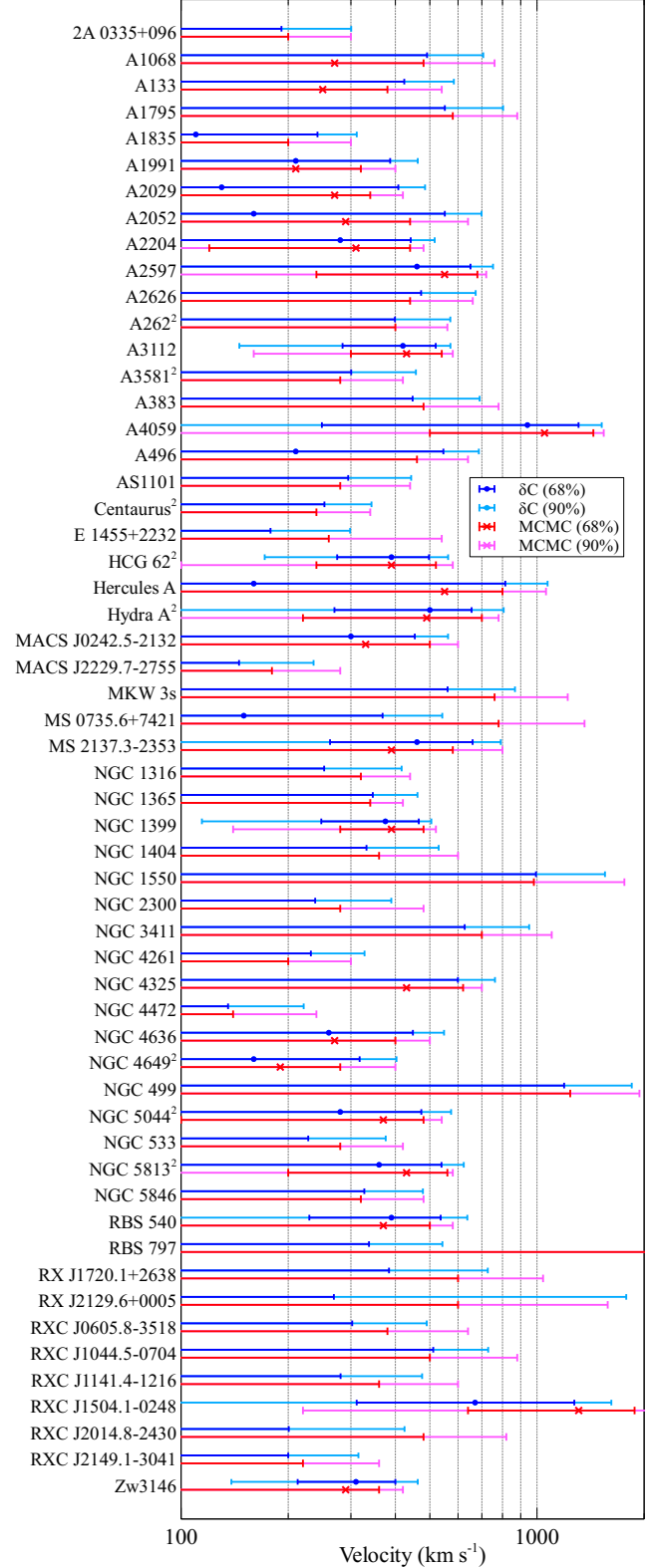


**Figure 2.** Error bars showing the  $1\sigma$  (68 per cent) and 90 per cent confidence regions for each object. Results using  $\delta C$  statistic and MCMC posterior probabilities are shown for each object. Objects marked with <sup>2</sup> include two spatial and/or thermal components in the spectral fit.

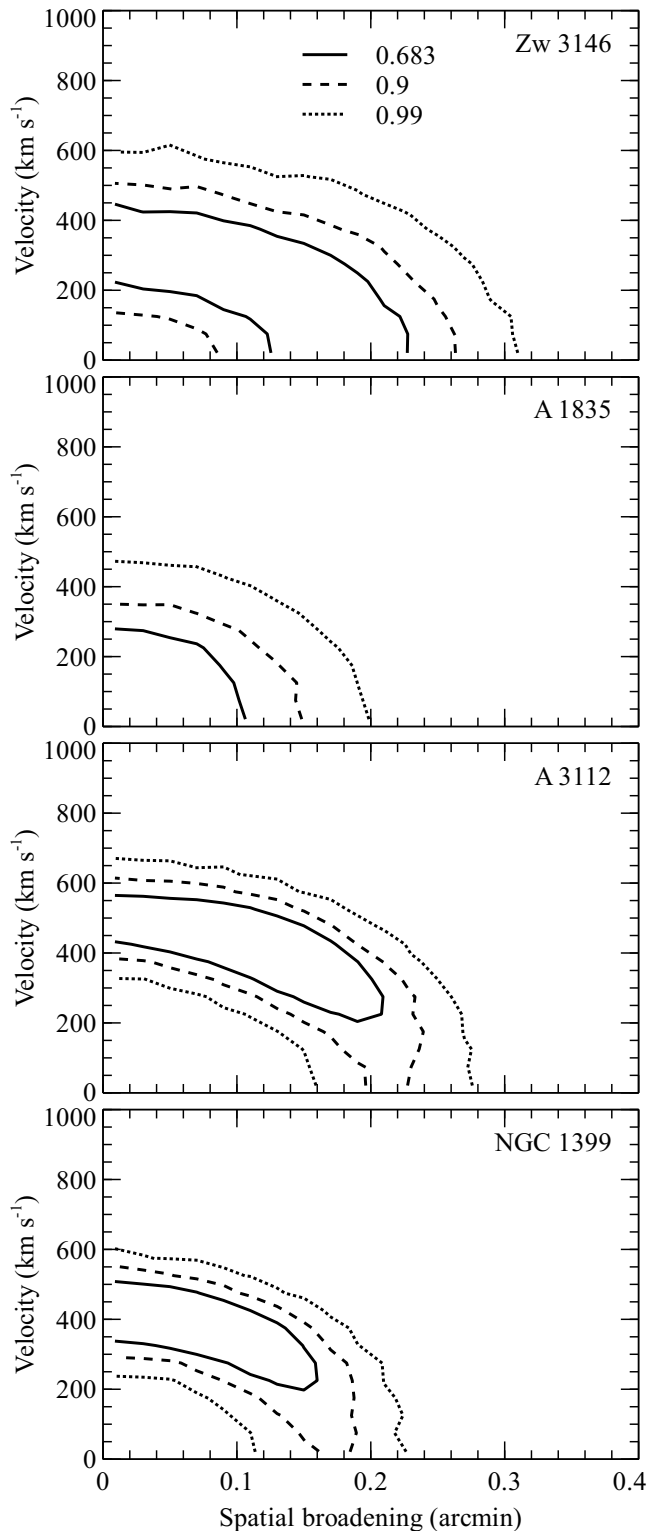


**Figure 3.** Confidence contours of velocity versus spatial broadening from the MCMC analysis. Contours show the 68.3, 90 and 95 per cent posterior confidence probabilities.

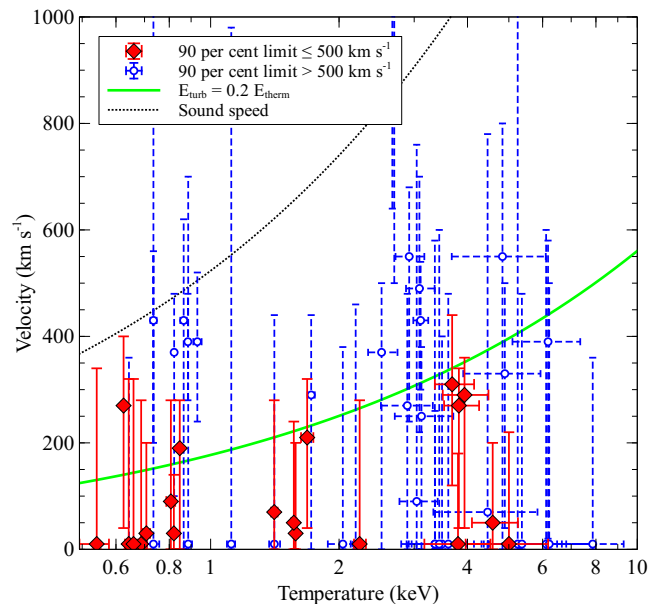


**Figure 4.** RGS temperature plotted against line width (using  $1\sigma$  MCMC uncertainties). We plot the upper temperature if more than one temperature component is fitted. The lower curve shows where the energy density in random motions is 20 per cent of the thermal energy density. The upper curve shows the sound speed.

### 2.2.1 Examining A 3112

Including a surface brightness profile in the modelling will fail if this profile does not accurately follow the emission lines that the RGS spectral fits are sensitive to. It might be thought that choosing a narrow band around Fe-L would give a good characterization of the line surface brightness. However, our testing has shown that even narrow bands often include too much continuum for many cool core clusters at larger radii, leading to over-correction of the line widths. The continuum at larger radii creates large wings in the response matrix which control the spectral fits. We demonstrate this in Fig. 5 which shows *Chandra* surface brightness profiles along the dispersion angle for an RGS observation of A 3112. The profiles are shown in a band tuned to the peak of the Fe-L emission (band B in Fig. 6) and the sum of two bands either side (bands A and C). The profiles are made in 1 arcsec bins along the dispersion angle, selecting the cross dispersion angle between  $-0.45$  and  $0.45$  arcmin. They are scaled by the number of counts in each band in an annulus from 1.4 and 1.9 arcmin radius.

The surface brightness profiles continue to decline smoothly to large radii in both the Fe-L and continuum-like bands. If the profiles in the bands are subtracted (Fig. 5 bottom panel), the continuum-subtracted Fe-L emission is seen to be more compact, without the long tails at large radii. The strong Fe-L emitting region corresponds roughly to where the temperature drops below 3 keV in the cluster.

We used the Fe-L ‘On’ (B band) profile to create response matrices using the ‘angdistset’ option to the RGSRMFGEN response generation tool. This option broadens the response matrix to account for the broadening due to the dispersion axis profile given. We input the profiles between dispersion angles between  $-4$  and  $4$  arcmin. This was done for each of the A 3112 datasets 0105660101, 0603050101 and 0603050201, as the dispersion angles were different in each case. The spectra and response matrices were combined with RGS COMBINE and fitted in XSPEC. In this case we ob-

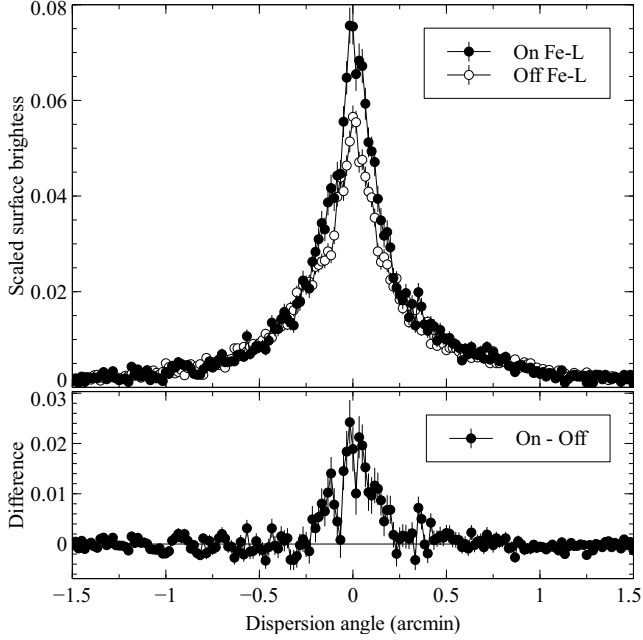


**Figure 5.** (Upper panel) *Chandra* surface brightness profile along the dispersion direction for the *XMM* 0603050101 observation for A 3112. The profiles are shown in the rest frame Fe-L (B-band, ‘On’) and in the spectral region either side (A and C, ‘Off’) and are normalized at angles of 1.37 to 1.9 arcmin. (Lower panel) Continuum-subtracted Fe-L emission, computed from difference between the B-band Fe-L and A+B profiles.

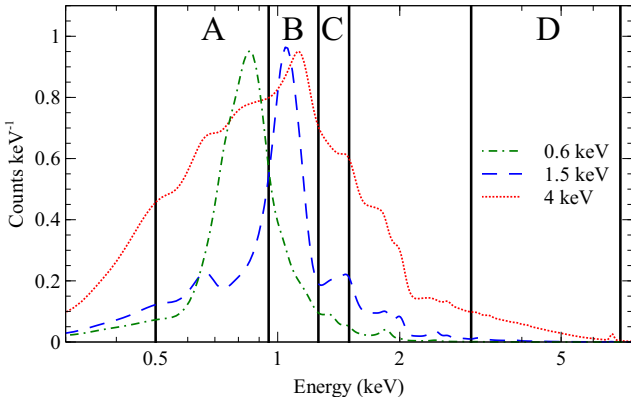


**Figure 6.** *Chandra* bands used for making line images for RGS analysis. Model spectra at example temperatures and  $0.5 Z_{\odot}$  are plotted. The effect of redshift were included.

tained a best fitting broadening of  $0 \text{ km s}^{-1}$  and an upper limit of  $175 \text{ km s}^{-1}$  (90 per cent confidence). The C-statistic for the best fit in this case is 4148 with 4064 degrees of freedom. Our upper limit is roughly consistent with those of Bulbul et al. (2012), who found  $\sim 200 \text{ km s}^{-1}$ .

Next, we instead used the continuum-subtracted Fe-L profile (bottom panel of Fig. 5) to create broadened response matrices, taking the values between dispersion angles of  $-0.4$  and  $0.4$  arcmin, where the signal appears significant. A velocity broadening of  $411 \pm 68 \text{ km s}^{-1}$  ( $1\sigma$ ) is obtained using this dispersion profile. If we discard the negative values after the continuum subtraction, we obtain a value of  $386 \text{ km s}^{-1}$  instead. Both of these values are consistent with the confidence contours from the pure RGS spec-

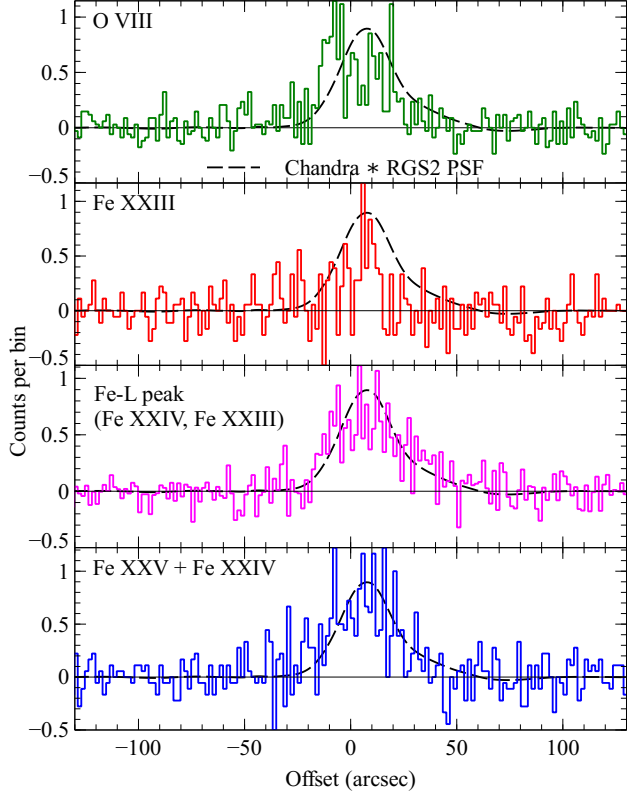


**Figure 7.** Continuum-subtracted profiles in the cross-dispersion directory for various lines from A 3112. We also plot the *Chandra* Fe-L continuum-subtracted profile convolved with the RGS2 cross-dispersion PSF at  $\beta = 0.055$ . For O VIII in the 1st panel we extract the line from the wavelength range  $20.35\text{--}20.52\text{\AA}$  and use both  $(20.05\text{--}20.22, 20.52\text{--}20.69)\text{\AA}$  as background. For the 2nd panel we use  $12.54\text{--}12.71\text{\AA}$  as foreground and  $12.72\text{--}12.90\text{\AA}$  as background. For the 3rd panel we use  $11.75\text{--}12.36$  and  $(11.37\text{--}11.50, 11.62\text{--}11.75)\text{\AA}$  as foreground and background, respectively. For the bottom 4th panel, we use  $11.32\text{--}11.49\text{\AA}$  as the foreground and  $11.14$  to  $11.31\text{\AA}$  as the background.

tral fitting shown in Fig. 3. The C-statistic for the best fit with this response matrix is 4103. When fitting for the spatial broadening (Section 2.1), we obtained the same fit statistic.

### 2.2.2 Systematic errors

There are a number of possible systematic errors to consider. Firstly, the line width we measure is a function of several different emission lines, each of which may have different spatial broadening (and intrinsic width). *Chandra* X-ray images cannot separate these out spectrally. Even when not accounting for spatial extent, the signal we measure will be some sort of average signal. Secondly, the radius at which we normalise the continuum may affect the result (particularly if there still line emission near the normalisation radius). The band used to calculate the continuum may not be clean enough, for example if it contains emission lines. Another potential problem is that the profile we input into the response generator needs to be truncated at a particular maximum offset, preferably where the tail of the surface of the brightness is zero but not including too much noise. Finally, the choice of background spectrum may have some effect, as in the previous section.

The *Chandra*-derived continuum-subtracted dispersion axis profile can be compared to those extracted in the cross-dispersion



**Table 4.** Results using *Chandra* imaging. The *Chandra* observations used to make the images are listed, as are the bands used to make the line image (Line) and continuum image (Cont.), the radial range where the surface brightness are normalised (Norm.) and the maximum offset of the profile along the dispersion direction when convolved with the response matrix. The background used for the spectral fitting (Bg) is either from the observation (O) or from a template (T). The velocities shown are limits or measurements with  $1\sigma$  or 90 per cent uncertainties. \*Selected background regions were chosen within these radii.

System	<i>Chandra</i> datasets	Line	Cont.	Norm. (arcmin)	Max. offset (arcmin)	Bg	Velocity (km s <sup>-1</sup> ) 1 $\sigma$	Velocity (km s <sup>-1</sup> ) 90 per cent
A 1068	1652	B	A,C	0.5–1.0*	$\pm 0.3$	O	< 500	< 690
		B	A,C	0.5–1.0*	$\pm 0.3$	T	< 368	< 566
A 1835	6880 6881 7370	B	A,C	0.8–1.4*	$\pm 0.5$	O	< 150	< 235
		B	A,C	0.8–1.4*	$\pm 0.5$	T	< 134	< 211
A 2029	891 4977	B	A,C	0.5–1.3*	$\pm 0.4$	O	< 285	< 375
		B	A,C	0.5–1.3*	$\pm 0.4$	T	< 372	< 446
A 2204	499 6104 7940	B	A,C	0.4–0.6	$\pm 0.25$	O	$278^{+120}_{-135}$	< 475
		B	A,C	0.4–0.6	$\pm 0.25$	T	$278^{+113}_{-135}$	< 465
A 2597	922 6934 7329	B	A,C	0.8–1.2	$\pm 0.5$	O	$480 \pm 120$	$480^{+190}_{-210}$
		B	A,C	0.8–1.2	$\pm 0.5$	T	$445 \pm 115$	$445^{+175}_{-200}$
		B	D	1.2–1.5	$\pm 1.0$	T	$330^{+128}_{-161}$	< 537
		B	D	2.0–2.5	$\pm 1.0$	T	< 410	< 490
A 3112	2216 2516	B	A,C	1.4–1.9	$\pm 0.4$	O	$411 \pm 68$	$411 \pm 115$
		B	A,C	1.4–1.9	$\pm 0.4$	T	$438 \pm 65$	$438 \pm 110$
		B	A,C	1.4–1.9	$\pm 1.0$	T	$337 \pm 80$	$337^{+120}_{-139}$
		B	A,C	2.8–3.4	$\pm 1.0$	T	$331 \pm 81$	$331^{+122}_{-141}$
		B	A,C	2.8–3.4	$\pm 1.6$	T	$350 \pm 80$	$350^{+122}_{-138}$
		B	D	1.4–1.9	$\pm 1.0$	T	$371 \pm 74$	$371 \pm 126$
		B	D	2.8–3.4	$\pm 1.0$	T	$277^{+81}_{-95}$	$277^{+130}_{-180}$
		A,B,C	D	1.4–1.9	$\pm 1.0$	T	$373 \pm 74$	$373^{+117}_{-126}$
E 1455+2232	543 4192 7709	A,B,C	D	2.8–3.4	$\pm 1.0$	T	$280^{+80}_{-95}$	$280^{+129}_{-180}$
		A,B,C	D	0.5–0.9	$\pm 0.3$	O	< 180	< 304
		A,B,C	D	0.5–0.9	$\pm 0.3$	T	< 200	< 345
Hydra A	4969 4970	B	A,C	0.8–1.6*	$\pm 1.0$	O	< 510	< 640
		B	A,C	0.8–1.6*	$\pm 1.0$	T	$504^{+192}_{-211}$	$504^{+320}_{-405}$
MS 2137.3-2353	928 4974 5250	A,B,C	D	0.3–0.6	$\pm 0.2$	O	$450 \pm 200$	$450^{+335}_{-410}$
		A,B,C	D	0.3–0.6	$\pm 0.2$	T	$375 \pm 230$	< 723
NGC 1399	319 9530	A,B	C	0.4–0.6	$\pm 0.4$	O	$325^{+65}_{-75}$	$325^{+114}_{-128}$
		A,B	C	1.2–1.5	$\pm 1.0$	T	$358 \pm 76$	$358^{+101}_{-57}$
		A,B	C	1.6–2.3	$\pm 1.0$	T	$370 \pm 75$	$370 \pm 125$
		A	C	1.6–2.3	$\pm 1.0$	T	$356 \pm 75$	$356 \pm 130$
		A,B	C	1.6–2.3	$\pm 1.5$	T	$382 \pm 75$	$382 \pm 120$
NGC 4636	3926 4415	A,B	C	1.3–1.5	$\pm 1.0$	O	$432^{+71}_{-80}$	$432^{+117}_{-135}$
		A,B	C	1.3–1.5	$\pm 1.0$	T	$581^{+65}_{-60}$	$581 \pm 103$
Zw 3146	909 9371	B	A,C	0.7–1.7*	$\pm 0.5$	O	< 290	< 370
		B	A,C	0.7–1.7*	$\pm 0.5$	T	< 289	< 360

direction from the RGS observations themselves. However, unless the cluster is symmetric they should not necessarily be the same. Fig. 7 shows the cross-dispersion surface brightness profiles in four different lines, subtracting the continuum from adjacent spectral regions. Also shown on each plot is the *Chandra* continuum-subtracted Fe-L dispersion axis profile convolved with the RGS2 cross-dispersion PSF. The plot shows that for the three strongest lines, there is reasonable agreement with the *Chandra* profile. For Fe XXIII, the line appears narrower than the *Chandra* profile. This is probably because it is emitted from the cooler material in the cluster, located in the very central regions. This line is relatively weak and is unlikely to contribute significantly to the line width signal when fitting the spectrum.

We can check how the continuum-subtracted profiles from *Chandra* depend on the choice of spectral bands. Fig. 8 shows profiles where different continuum and line bands were used, and different radii for normalisation of the continuum and line bands. It can be seen that the continuum band makes little difference to the continuum-subtracted line profile. The line band has some effect,

where the two softer line bands have stronger peaks in the central region than the B band profile. The normalisation radius has little effect when the bands are close in energy (B and A+C), but does affect the result if they are further away in energy (B and D).

We examined the effect of these possible systematic problems by repeating the A3112 analysis but varying some of the choices we made. Using a template background instead of the observation-derived background increased the best-fitting broadening by  $30 \text{ km s}^{-1}$  in this object. The line width decreased by  $100 \text{ km s}^{-1}$  when the dispersion axis angular range was increased from  $-0.4$  to  $0.4$  to  $-1$  to  $1$  arcmin, using a template background. Increasing the angular range still further to  $1.6$  arcmin increased the line width slightly by  $20 \text{ km s}^{-1}$ . If we instead increased the radii where the line and continuum profiles were normalised from  $1.4$ – $1.9$  to  $2.8$ – $3.4$  arcmin, this decreased the velocity by only  $6 \text{ km s}^{-1}$ . The difference is more dramatic if a continuum band is chosen which is substantially different in energy from the line emitting band. Using band D as a continuum band, the broadening decreased from  $370$  to  $280 \text{ km s}^{-1}$  when going from the inner to outer

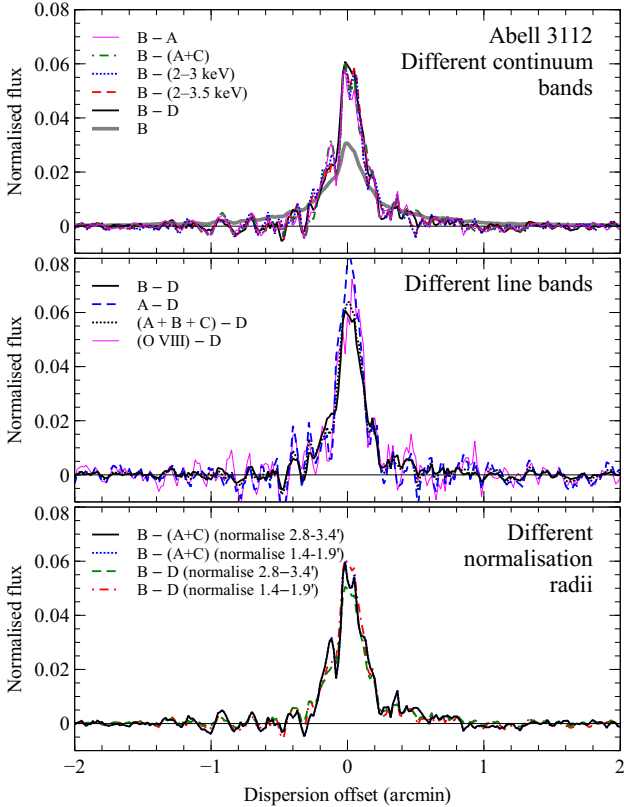


**Figure 8.** Comparison of continuum subtracted profiles. The top panel show the effect of using different continuum bands (or none). The centre panel shows the effect of using different foreground bands. The bottom panel shows the effect of normalising the foreground and background in two different radial ranges. The profiles have been normalised to have a total signal of unity. They have been smoothed using a running average, taking the mean of each point with its two neighbours. The key shows the line and continuum bands as a subtraction.

normalisation radii. The inner region value is close to that when using the adjacent A and C energy bands as continuum. The effect of the choice of band containing the line emission can be examined. If we combine the A, B and C bands, using D as the continuum, there is negligible change to the line width than when just using B.

These tests show that the broadening we obtain can change by around  $160 \text{ km s}^{-1}$  depending on the choice of bands, background and radii. This is the likely systematic uncertainty on any results of broadening. The range of values we obtain for A 3112 ( $180 - 500 \text{ km s}^{-1}$ ) is consistent with the confidence contours shown in Fig. 3.

### 2.2.3 Other targets

We used this technique to include the surface brightness profile for several targets (listed in Table 4). Unfortunately it cannot be straightforwardly applied to every object as certain conditions must be able to be met. Firstly, the core of the centre of the object must have strong line emission and the outer parts must not. This is achieved in cool core clusters. It should be unambiguous where the cool line-emitting region starts and the continuum region ends. We used *Chandra* temperature maps to help identify where to normalise the continuum and line profiles. Secondly, if the object has line emission in different emission lines which are spatially re-

solved (for example, due to a temperature gradient over a large cool core) then the subtraction process often does not work, as the emission lines move through different bands. This problem is seen in the Centaurus, A 2052 and A 3581 clusters, where the subtracted profiles are zero at large radii, become negative and then become positive. Finally, the object should have good *Chandra* data. The small PSF of *Chandra* means that we do not have to deconvolve it from the dispersion direction profile and enables us to easily remove point sources. A future analysis using *XMM* data should be possible if its PSF is accounted for.

For some distant objects without deep *Chandra* observations the bands A, B and C are rather narrow and contain too few counts. For these objects we therefore use A, B and C as foreground bands and a high-energy D band as a continuum band. For cooler objects, such as elliptical galaxies, the cool core is at lower temperatures. The Fe-L peak moves into the A band, instead of the B band. We therefore use the A and B bands as the foreground bands in these objects and band C as the background continuum band. The bands used for each observation are listed in Table 4. As with A 3112, when convolving the continuum-subtracted emission line profile with the response matrices, we trim the profiles in dispersion angle where we do not see any signal above zero. These angular ranges are also listed in Table 4.

Our velocity results are listed in Table 4, showing the statistical uncertainties at the  $1\sigma$  and 90 per cent confidence levels. These measurements or limits were made using the  $\delta C$  approach. The same free parameters were used as when fitting in the previous section (except for the spatial broadening).

There are a mixture of improved upper limits (such as A 1835 and Zw 3146) and possible detections of broadening of the emission lines at  $300$  to  $500 \text{ km s}^{-1}$  (e.g. A 3112 and NGC 4636).

We also investigate some of the possible systematic effects for the sample. For each object we compare the results using template and observation-derived spectral backgrounds. In some cases this can make large changes to the results (e.g. Hydra A, NGC 4636 and A 1068), but for the remainder the effect is small. For NGC 1399 we investigate the choice of emission line band, normalisation radius and extent of the profile included in the convolution. For this object the range in velocities is around  $75 \text{ km s}^{-1}$ , smaller than for A 3112. We also examine the choice of continuum in A 2597 and the maximum dispersion angle included in the PSF convolution. Similarly to A 3112, there is a range of  $\sim 150 \text{ km s}^{-1}$  in the velocity broadening, depending on the choice of parameters.

### 2.3 Other methods

The RGS instruments provide high spectral resolution images of the source in the cross-dispersion direction. The shape of the source in the cross-dispersion direction in a particular line can be directly measured from these images. If the source is close to symmetric in the dispersion and cross-dispersion directions, then the cross-dispersion profile can be used to account for the contribution of the extent to the line width. This method requires that there are enough photons in the lines for the extent to be measured (See e.g. Fig. 7). For many targets, this will not be the case for individual lines.

A more complete approach would be to use Monte Carlo modelling of the cluster to fit all the observations, including imaging and the cross-dispersion information. Peterson et al. (2007) have used smoothed particles to model galaxy clusters, but have not yet used this technique to extract velocity width information.

### 3 DISCUSSION

The measurements and limits on the velocity width we present are of the X-ray coolest gas, as measured using Fe-L and O VIII, characterised by gas at 3 keV or below. When *ASTRO-H* (Takahashi et al. 2010) is launched, its microcalorimeter will be most sensitive to the width of the Fe-K emission lines as it has fixed spectral resolution in terms of energy. Fe-K emission characterizes the hotter gas, which may give a wider range of velocities than the cooler material that the RGS is sensitive to.

It is possible that the coolest gas may have sufficient inertia to avoid major velocity flows (or it would be destroyed by them). Previous results using RGS and *Chandra* have shown that the X-ray coolest gas consists of X-ray cool clumps embedded in a hotter medium (Sanders et al. 2009, 2010a), providing that the two phases are in pressure balance. *ASTRO-H* will give complementary data on the hotter, volume-filling component.

The turbulence or velocity structure of the coolest gas may be due to a number of different physical effects. The active galactic nucleus (AGN) may be generating kinetic feedback in its environment, including jets and bubbling (Brüggen et al. 2005; Heinz et al. 2010). Cold fronts, if they require large flows (e.g. Ascasibar & Markevitch 2006), may generate velocity broadening if they are within the spatial region examined by our analysis. We note that the physical region probed by our analysis is different for each of our objects. It is dependent on the redshift of the object as our extraction region is a fixed angular size and the physical extent of the line-emitted material within this aperture.

The velocities we measure with RGS are comparable to, or exceed, the velocity width of optical emission line gas (after converted the quoted full width at half maximum, FWHM, to  $\sigma$ ). Hatch et al. (2007) examined A 1068, A 262, A 496 and 2A 0335+096. Crawford & Fabian (1992) observed the objects AS 1101, A 2597 and A 496. Allen et al. (1992) measured line widths from A 1835, Zw 3146 and A 1068.

Some of our results are inconsistent with results from previous analyses of line widths. Our measurement of  $280 - 440 \text{ km s}^{-1}$  for A 3112 does not agree with the upper limit of  $200 \text{ km s}^{-1}$  of Bulbul et al. (2012) when they included the effect of the spatial distribution of the source. This is probably because the continuum was not subtracted from the surface brightness profile when computing the spatial broadening effect. In Sanders et al. (2011) we used *Chandra* spatially resolved maps to model expected line widths, to subtract from observed line widths. This analysis appears to have overestimated the spatial broadening effect in several objects. This can be seen by the disproportionate number of objects where the predicted line width is wider than the observed line width, although some would be expected if the intrinsic velocity broadening is low. One likely contributing factor is the finite bin size of the input maps used to create the simulated spectra. In our previous paper the spatial and implied velocity broadening were also not added in quadrature to obtain the observed broadening. Our new method avoids the problems caused by our previous modelling using spectral maps.

The velocities we obtain for NGC 5044 and NGC 5813 are consistent with those found by de Plaa et al. (2012) using both line widths and resonance scattering.

We note that for NGC 4636, the  $430 - 580 \text{ km s}^{-1}$  broadening we measure is apparently inconsistent with the  $100 \text{ km s}^{-1}$  upper limit inferred from the presence of resonance scattering (Werner et al. 2009). However, these values may still be in agreement if the broadening we measure is the result of ordered motion. The radio source is likely to produce a bipolar outflow which will give a

strong resonance scattering signal due to the low relative velocities of gas on either side. The emission lines, however, would be broadened by the difference in outflow velocities between each side. Alternatively, the disagreement may be because the spatial distribution of the line emission is not properly accounted for in our analysis. Although the *Chandra* surface brightness profile appears consistent with the location of the brightest and coolest part of the group ( $\sim 0.6 \text{ keV}$  temperature, in a  $0.3 \text{ arcmin}$  radius core, with  $1 \text{ arcmin}$  wings), the profiles of individual lines may be different in this rather complex source. Another possible uncertainty is that the resonance scatter results may be affected theoretical uncertainties on the relative strengths of the Fe XVII emission lines as a function of temperature (see e.g. Sanders et al. 2008).

In Section 2.1 we measured the velocities assuming that the line surface brightness could be fitted well by a Gaussian model. There will be a systematic uncertainty associated with this assumption. In the case of A 3112 this assumption is a reasonable one, as shown by the continuum-subtracted surface brightness profile in Fig. 5 and cross-dispersion line profiles in Fig. 7. The line width results for A 3112 from this method (Table 3 and Fig. 3) also agree well with the results using the technique using the *Chandra* surface brightness profiles (Table 4). Other objects with resolved or marginally-resolved line widths show good agreement between the methods, including NGC 1399, MS 2137, A 2204 and A 2597. The object with the largest difference between the methods is NGC 4636. This target has a complex morphology so the Gaussian assumption may not be good in this case.

Detailed spatially-resolved line profiles (measuring line widths and positions as a function of radius) will enable (Zhuravleva et al. 2012) the turbulent spectrum of the velocity field to be determined. We await the results from future X-ray missions flying high spectral resolution detectors, such as *ASTRO-H*, to examine line shapes in detail as a function of position.

In our analysis, we used both a conventional and a MCMC method for examining uncertainties on parameters. For most of our objects, the results agreed. The use of the affine-invariant MCMC sampler made it much easier to do the MCMC analysis compared to Metropolis-Hastings. With Metropolis-Hastings it is often difficult to choose an appropriate proposal distribution, leading to the parameter space being poorly sampled because of too many or too few rejections. The algorithm also has difficulty when parameters are strongly correlated. The affine-invariant MCMC analysis was not a complete success, however, because in several cases we had to increase the number of walkers to get agreement between the conventional and MCMC results. Some parts of parameter space were missed in the MCMC analysis for some objects. Therefore, it was much easier to get quick, robust and stable results using conventional techniques rather than MCMC. The advantage of the MCMC approach was that we were able to examine the correlations of each parameter with every other and with the fit statistic (e.g. Fig. 3). This allowed us to understand the modelling better. In a few cases, there are still divergent results between MCMC and the conventional technique, which may indicate that the C-statistic uncertainties are underestimated because of a tail in the posterior probability distribution.

### 4 CONCLUSIONS

We present limits or measurements of the velocity width of the soft X-ray emission for a sample of clusters and groups of galaxies, and elliptical galaxies, using data from *XMM* RGS. In our

analysis we take two different approaches to including the spatial broadening intrinsic to the RGS instruments. For all targets, we model the spatial broadening with a Gaussian component in the spectral modelling. For a subset of objects we also use a second approach where *Chandra* imaging data in a continuum-subtracted line-emitting band is used to model the spatial broadening.

Using Gaussian spatially modelling, for twenty of the targets we find upper limits on the velocity broadening of less than  $500 \text{ km s}^{-1}$  and find five targets with limits of  $300 \text{ km s}^{-1}$  or lower. There are some targets for which we detect velocity broadening with 90 per cent confidence between  $300$  to  $500 \text{ km s}^{-1}$ , including A 3112, HCG 62 and NGC 1399. NGC 4636 shows broadening if *Chandra* imaging is used in the spectral analysis.

## ACKNOWLEDGEMENTS

ACF acknowledges the support of the Royal Society. We thank Randall Smith for supplying the APEC code. We are grateful to an anonymous referee for comments which significantly improved this paper.

## REFERENCES

- Allen S. W. et al., 1992, *MNRAS*, 259, 67  
 Anders E., Grevesse N., 1989, *Geochim. Cosmochim. Acta*, 53, 197  
 Arnaud K. A., 1996, in Jacoby G. H., Barnes J., ed, *ASP Conf. Ser.* 101: *Astronomical Data Analysis Software and Systems V*, p. 17  
 Ascasibar Y., Markevitch M., 2006, *ApJ*, 650, 102  
 Balucinska-Church M., McCammon D., 1992, *ApJ*, 400, 699  
 Brinkman A. et al., 1998, in *Proceedings of the First XMM Workshop on Science with XMM*, <http://xmm.esac.esa.int/>  
 Brüggén M., Hoefl M., Ruszkowski M., 2005, *ApJ*, 628, 153  
 Bulbul G. E., Smith R. K., Foster A., Cottam J., Loewenstein M., Mushotzky R., Shafer R., 2012, *ApJ*, 747, 32  
 Crawford C. S., Fabian A. C., 1992, *MNRAS*, 259, 265  
 de Plaa J., Zhuravleva I., Werner N., Kaastra J. S., Churazov E., Smith R. K., Raassen A. J. J., Grange Y. G., 2012, *A&A*, 539, A34  
 Foreman-Mackey D., Hogg D. W., Lang D., Goodman J., 2012, [arXiv:1202.3665](https://arxiv.org/abs/1202.3665)  
 Goodman J., Weare J., 2010, *Communications in Applied Math.*, 5, 65  
 Hatch N. A., Crawford C. S., Fabian A. C., 2007, *MNRAS*, 380, 33  
 Heinz S., Brüggén M., Morsony B., 2010, *ApJ*, 708, 462  
 Lau E. T., Kravtsov A. V., Nagai D., 2009, *ApJ*, 705, 1129  
 Peterson J. R., Marshall P. J., Andersson K., 2007, *ApJ*, 655, 109  
 Sanders J. S., Fabian A. C., Allen S. W., Morris R. G., Graham J., Johnstone R. M., 2008, *MNRAS*, 385, 1186  
 Sanders J. S., Fabian A. C., Frank K. A., Peterson J. R., Russell H. R., 2010a, *MNRAS*, 402, 127  
 Sanders J. S., Fabian A. C., Smith R. K., 2011, *MNRAS*, 410, 1797  
 Sanders J. S., Fabian A. C., Smith R. K., Peterson J. R., 2010b, *MNRAS*, 402, L11  
 Sanders J. S., Fabian A. C., Taylor G. B., 2009, *MNRAS*, 396, 1449  
 Smith R. K., Brickhouse N. S., Liedahl D. A., Raymond J. C., 2001, *ApJ*, 556, L91  
 Takahashi T. et al., 2010, *Proc. of SPIE*, 7732, 77323J  
 Vazza F., Brunetti G., Gheller C., Brunino R., Brüggén M., 2011, *A&A*, 529, A17  
 Vazza F., Brunetti G., Kritsuk A., Wagner R., Gheller C., Norman M., 2009, *A&A*, 504, 33  
 Werner N., Zhuravleva I., Churazov E., Simionescu A., Allen S. W., Forman W., Jones C., Kaastra J. S., 2009, *MNRAS*, 398, 23  
 Zhuravleva I., Churazov E., Kravtsov A., Sunyaev R., 2012, *MNRAS*, 422, 2712